Research article

DOI: 10.1111/boc.201600080

Research article: To characterise the early phase of integrin-mediated adhesion in alveolar epithelial cells, the force spectroscopy method is revisited by a new theoretical approach predicting adhesion reinforcement in multiple bonds working non-cooperatively with homogeneous redistribution of the stretching force. The present results show that the multiple bond force spectroscopy method presently proposed enables detection of bond number and the impact of bond association on adhesion reinforcement.

Characterisation of cellular adhesion reinforcement by multiple bond force spectroscopy in alveolar epithelial cells

Ngoc-Minh Nguyen, Christelle Angely, Sofia Andre Dias, Emmanuelle Planus, Marcel Filoche, Gabriel Pelle, Bruno Louis and Daniel Isabey

Biol. Cell (2017) **109**, 1–18

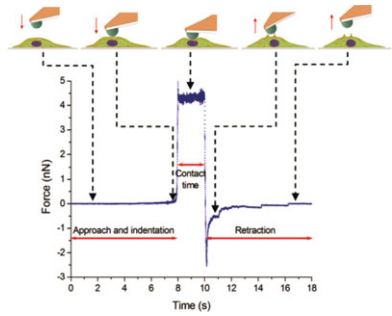

Biol. Cell 2017, 109(7), DOI:10.1111/boc.201600080

Biol. Cell (2017) **109,** 1–18 DOI: 10.1111/boc.201600080

Research article

Characterisation of cellular adhesion reinforcement by multiple bond force spectroscopy in alveolar epithelial cells

Ngoc-Minh Nguyen*†‡[2], Christelle Angely*†‡[2], Sofia Andre Dias*†‡, Emmanuelle Planus§, Marcel Filoche*†‡‖, Gabriel Pelle*†‡#, Bruno Louis*†‡ and Daniel Isabey*†‡[1]

*Inserm, U955, Equipe 13, Biomécanique & Appareil Respiratoire, Créteil Cedex F-94010, France, †Université Paris Est, UMR S955, UPEC, Créteil Cedex F-94010, France, ‡CNRS, ERL 7240, Créteil Cedex F-94010, France, §Institute for Advanced Biosciences (IAB), Centre de Recherche UGA/Inserm U1209/CNRS UMR 5309, La Tronche, 38700, France, ‖Laboratoire de Physique de la Matière Condensée, Ecole Polytechnique, CNRS, Université Paris Saclay, Palaiseau 91128, France, and #AP–HP, Groupe Hospitalier H. Mondor – A. Chenevier, Service des Explorations Fonctionnelles, Créteil Cedex F-94010, France

Background Information. Integrin-mediated adhesion is a key process by which cells physically connect with their environment, and express sensitivity and adaptation through mechanotransduction. A critical step of cell adhesion is the formation of the first bonds which individually generate weak contacts (~tens pN) but can sustain thousand times higher forces (~tens nN) when associated.

Results. We propose an experimental validation by multiple bond force spectroscopy (MFS) of a stochastic model predicting adhesion reinforcement permitted by non-cooperative, multiple bonds on which force is homogeneously distributed (called parallel bond configuration). To do so, spherical probes (diameter: 6.6 μm), specifically coated by RGD-peptide to bind integrins, are used to statically indent and homogenously stretch the multiple bonds created for short contact times (2 s) between the bead and the surface of epithelial cells (A549). Using different separation speeds (v = 2, 5, 10 μm/s) and measuring cellular Young's modulus as well as the local stiffness preceding local rupture events, we obtain cell-by-cell the effective loading rates both at the global cell level and at the local level of individual constitutive bonds. Local rupture forces are in the range: $f^* = 60 - 115$ pN, whereas global rupture (detachment) forces reach $F^* = 0.8 - 1.7$ nN. Global and local rupture forces both exhibit linear dependencies with the effective loading rate, the slopes of these two linear relationships providing an estimate of the number of independent integrin bonds constituting the tested multiple bond structure (~12).

Conclusions. The MFS method enables to validate the reinforcement of integrin-mediated adhesion induced by the multiple bond configuration in which force is homogeneously distributed amongst parallel bonds. Local rupture events observed in the course of a spectroscopy manoeuver (MFS) lead to rupture force values considered in the literature as single-integrin bonds.

Significance. Adhesion reinforcement permitted by the parallel multiple bond association is particularly challenging to verify for two reasons: first, it is difficult to control precisely the direction of forces experimentally, and second, because both global and local bond rupture forces depend on the effective loading rate applied to the bond. Here, we propose an integrin-specific MFS method capable of detecting bond number and characterising bond configuration and its impact on adhesion strength.

[1]To whom correspondence should be addressed (email: daniel.isabey@inserm.fr)
[2]These authors contributed equally to this work.
Key words: Actin cytoskeleton, Atomic Force Microscopy, Integrins, Multiple bond rupture, RGD-coating.

Abbreviations: AEC, alveolar epithelial cells; AFM, atomic force microscopy; ECM, extracellular matrix; KS, Kolmogorov–Smirnov; MFS, multiple bond force spectroscopy; MTC, magnetic twisting cytometry; RGD, arginine–glycine–aspartic acid.

Introduction

It is widely recognised that forces acting on cells govern important regulatory events and thus are key factors in biological processes. Force transmission across plasma membrane is mediated by mechanoreceptors such as integrins which are present in most matrix-related adhesions sites (Schwarz and Gardel, 2012). By relating intracellular structure (the cytoskeleton) to extracellular matrix (ECM) ligands, integrin–ligand binding plays a central role in the force-control of cell adhesion (LaCroix et al., 2015) and in the ability of cells to sense and to adapt to their mechanical environment (Discher et al., 2005). Integrins not only transmit signals to cells in response to the cellular attachment to extracellular environment (outside-in signalling) but also infer intracellular cues to alter their interaction with extracellular environment (inside-out signalling) (Liu et al., 2000). This is why integrins and more precisely the receptor–ligand binding are key pieces of mechanotransduction, a process by which cells convert physical forces into changes in intracellular biochemistry (Ingber, 2003). Thanks to these integrin-specific protein–protein linkages, and to other types of intracellular structures such as the tensed cytoskeleton, physical forces contribute to cell regulation and to cell sensitivity as efficiently as – and even more rapidly than – biochemical processes (Wang et al., 2009).

Force regulation of cell adhesion is possible because integrin–ligand junctions are non-covalent junctions which collectively can sustain high mechanical strength of the order of 10 nanoNewton (Palecek et al., 1997) but individually generate weak contacts resisting only several tens of picoNewton before subsequent strengthening (Lo Schiavo et al., 2012). Both dynamic adhesion models and studies of cell sensitivity on substrates of different stiffness show that nascent adhesion sites, *i.e.* the early stage of development, enable cells to be sensitive to mechanical environment and exhibit a stiffness (or intracellular tension) dependent reinforcement while they are still in a reversible state (Choquet et al., 1997; Féréol et al., 2009). To counterbalance their relative weakness on adhesion sites, the mechanosensitive bonds have to work together in order to sustain force. Indeed, subsequent adhesion strengthening occurs through integrin clustering and linkage to the cytoskeleton (Cluzel et al., 2005; Taubenberger et al., 2007). Many bond structures can be considered but we focus here on two major configurations as models of initial adhesion reinforcement: the parallel and the zipper configurations (Williams, 2003) because they take into account two opposed situations in terms of force distribution on bonds, namely the fully homogeneous or fully heterogeneous force distributions, respectively, which lead to quite different levels of adhesion reinforcement (Isabey et al., 2013). Our aim is to assess experimentally some key aspects of the multiple bond theory for parallel configuration on alveolar epithelial cells (AEC) using (i) atomic force microscopy (AFM) which is the appropriate technique to study the parallel bond configuration (Sulchek et al., 2005; Rankl et al., 2008) and (ii) a modified force spectroscopy technique called multiple bond force spectroscopy (MFS) to assess, on the same force–distance curves, the essential features of multiple bonds.

In spite of numerous studies to characterise single bonds notably by force spectroscopy (Li et al., 2003; Sun et al., 2005; Evans and Kinoshita, 2007), the predicted behaviour of multiple receptor–ligand bonds (Williams, 2003; Isabey et al., 2013) has been rarely validated experimentally for integrins (Sulchek et al., 2005; Rankl et al., 2008). To do so, we use coated spherical micrometer probes to mimic a small matrix specifically recognised by integrins while using short contact times and quasi-static conditions of approach, indentation and retraction. This procedure enables us to compare the overall strength of a newly generated integrin-specific multiple bond system created at the probe–cell interface to that of its constitutive individual bonds. Through a precise estimate of the loading rates specific to the global and local rupture events, the MFS method allows us to determine the characteristics of the multiple bond system – including the bond number – by comparing them with the properties of single bonds which collectively contribute to the reinforcement of the multiple bond.

Results

In order to assess the integrin-specificity of the probe coating (see Material and Methods), comparative measurements of detachment forces were preliminary performed with the same probe while testing non-specific and specific coating conditions. The four conditions tested are: (i) the bare probe cleaned by Triton and then Ethanol (non-specific coating), (ii) the

probe cleaned by air plasma treatment (non-specific coating), (iii) the probe cleaned by plasma treatment and coated with BSA (non-specific coating) and (iv) the probe cleaned by air plasma treatment and coated with arginine–glycine–aspartic (RGD) 2.5 mg/ml (integrin-specific coating). The data obtained with these four conditions on A549 cells are shown in Figure 1: (i) for the raw data, where four typical force–distance curves obtained in four cells are presented in Figure 1A, (ii) for the detachment forces measured in a large population of cells in Figure 1B. One can observe in Figure 2A that the amplitude of the force–distance curve obtained in condition (iv) is much higher than the three other curves, revealing that integrin-specific coating results in higher detachment forces, and a higher number of local rupture events (Figure 1A). Clearly, integrin-specific coating of the bead enables assessment of integrin-specific binding in A549 cells.

Cell adhesion parameters and cell mechanical properties are measured through these integrin-specific linkages in wide groups of AEC ($n \geq 100$; see Table 1). These measures aim at evaluating the effects of three different probe displacement speeds (v = 2, 5, 10 μm/s) using identical speeds for the indentation and separation phases. We find that maximal detachment force noted F^* (Figure 2A) and work of adhesion W_{adh} (Figure 2B) tend to increase when the separation speed is increased. Nevertheless, the spread of results is important [see the large standard deviations (SD) of F^* and W_{adh} shown by Table 1] and reflects the intercellular variability since each value represents a different cell. Intercellular variability is also important for the measured Young's modulus E_{cell} values – measured in the indentation phase – although the differences in E_{cell} measured between the three indentation speeds are not systematically significant (Figure 2C). Because of this large intercellular biological variability, the evolutions of the mean values of F^* and W_{adh} are not linear with separation speeds (see Figures 2A and 2B and Table 1). Noteworthy, the variability in E_{cell} results in variability of the global loading rate through Eq. (10) written at the cellular level: $r_f (= k_{Cell} v)$ with k_{Cell} the cellular stiffness defined by: $k_{Cell} = E_{cell} \times \delta$ (in pN/μm) and δ a characteristic distance scale. Thus, intercellular variability of the Young's modulus results in loading rate variability which in turns contributes to the measured variability in F^*(through for instance Eq.

Figure 1 | Specificity of RGD coating seen on force-distance curves and detachment forces

The effect of three non-specific and one integrin-specific probe coating conditions shown: in (**A**) on four typical force–distance curves obtained in four different alveolar epithelial cells (A549) with (i) bare probe (green curve), (ii) plasma treatment (orange curve) and (iii) plasma treatment with BSA coating (brown curve), (iv) plasma treatment + RGD 2.5 mg/ml coating (purple curve). In (**B**) on detachment forces F^*(in nN) obtained throughout a wide number of cells. Dot in box marks the mean value, whisker bars the ±SD values, and horizontal bar in box gives the median value. For F^*, the integrin specific probe coating results in significant differences with the three non-specific coating conditions.

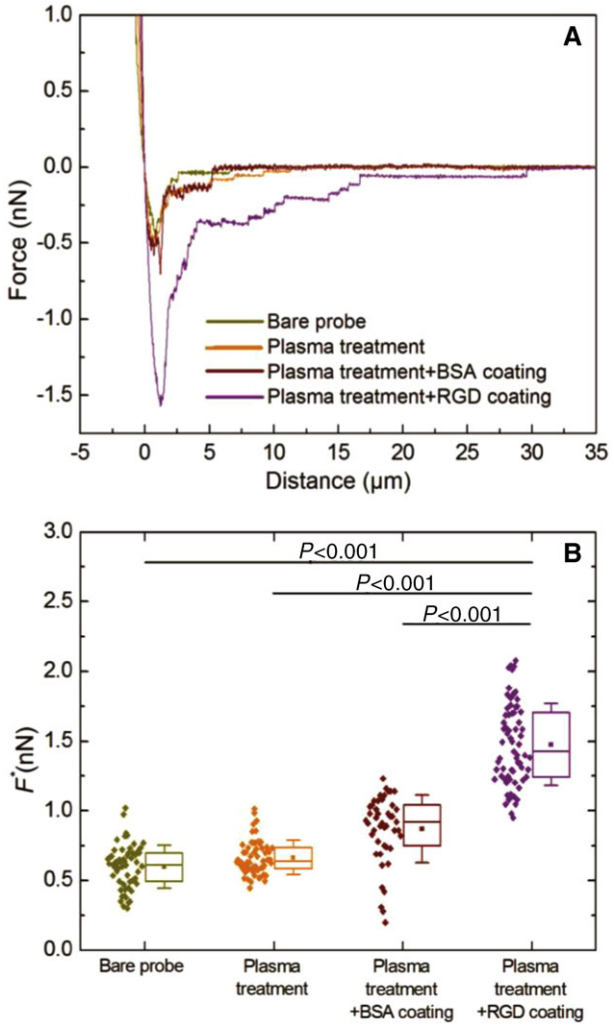

Figure 2 | See Legend on next page

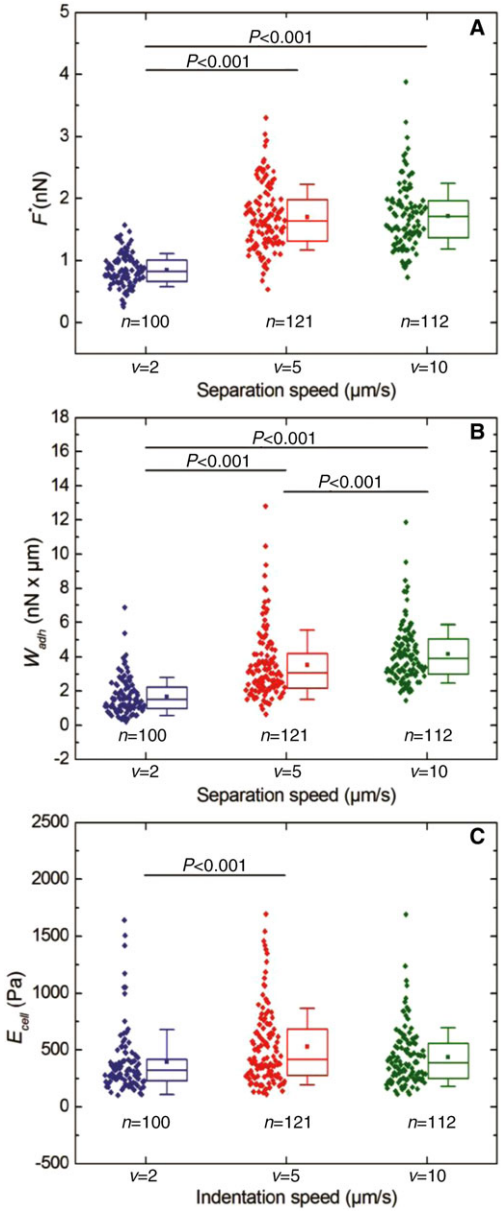

Figure 2 | Detachment force F^*, work of adhesion W_{adh} and Young's modulus E_{cell} are obtained throughout a wide number of cells for three different speeds of either separation (for F^* and W_{adh}) or indentation (for E_{cell})

(**A**) Maximal detachment force (F^*in nN) and (**B**) work of adhesion (W_{adh} in nN $\times$ μm) are measured cell-by-cell during retraction in A549 cells for three different predetermined separation speeds v, namely v = 2 μm/s (blue diamonds); 5 μm/s (red diamonds); 10 μm/s (green diamonds). The numbers of tested cells are: at $v = 2$ μm/s, $n = 100$; at v = 5 μm/s, $n = 121$, at v = 10 μm/s, $n = 112$. The squares in rectangular boxes mark the mean value, whisker bars the ±SD values and the horizontal line in each box gives the median value. Black horizontal bars display statistical significance ($p < 0.005$). (**C**) Young's modulus (E_{cell} in Pa) measured cell-by-cell during indentation in A549 cells for three different predetermined indentation speeds, v, namely v = 2 μm/s (blue diamonds); 5 μm/s (red diamonds); 10 μm/s (green diamonds). Number of tested cells is: at v = 2 μm/s, $n = 100$; at v = 5 μm/s, $n = 121$, at v = 10 μm/s, $n = 112$. Square in rectangular box marks the mean value, whisker bars the ±SD values, and horizontal line in box gives the median value. Black horizontal bar displays statistical significance ($p < 0.005$).

(7)) and W_{adh} but intrinsic variability of the molecular bond systems could also contribute. Interestingly, the closeness between median values and mean values (Figures 2A and 2B) suggests that values of F^* and W_{adh} are close to a normal or Gaussian distribution which remains consistent with the assumption that data dispersion arises from intercellular biological variability (Cardinal, 2015). The characteristic distance scale δ has been estimated cell by cell from the ratio W_{adh}/F^* (see Table 1). The method to estimate δ appears more reliable than a rough estimation of the slope (derivative) on the force–distance curve which is not constant. The mean (±SD) global loading rate values so calculated are presented in Table 1. The advantage of the present approach is to provide a cell-specific estimate of the three interdependent parameters: F^*, W_{adh}, and $r_f (= k_{Cell} v)$.

The relationship ($F^* - \ln r_f$) between the maximal detachment force measured during separation and the global loading rate are plotted in Figure 3 for several hundred cells (see Table 1), tested with three separation speeds. We also plot on the same graph the mean values of F^* (±SD) and r_f (±SD) which represent the most likely values (±SD) for each group (Table 1). The whole set of data can be fitted with a linear regression line plotted in Figure 3 (slope and intercept are given in Table 2). The slope of the linear regression line leads to the reference force F_β (= 342 pN) and the intercept at r_f= 1 pN/s leads to the natural dissociation rate, K^0_{off} (= 0.16 s^{-1}). For the regression line (not shown) relating the most likely values of F^* and r_f obtained in each group, we find close values: F_β(= 467 pN) and K^0_{off}(= 0.43 s^{-1}) (see Table 2).

Table 1 | Mean values ±SD of global mechanical (E_{cell}) and adhesion parameters ($F^*$and W_{adh}) determined in '*n*' different cells and at three different predetermined indentation/separation speeds v = 2, 5, 10 μm/s. The characteristic distance of cell deformation is estimated from $\delta = W_{adh}/F^*$ in each cell. The global loading rate r_f is calculated cell-by-cell from the product: $r_f = E_{cell} \times \delta \times v$, as described in the *Results* section

	$v = 2$ μm/s ($n = 100$)		$v = 5$ μm/s ($n = 121$)		$v = 10$ μm/s ($n = 112$)	
	Mean	SD	Mean	SD	Mean	SD
Global detachment force F^* (nN)	0.84	0.27	1.7	0.53	1.71	0.53
Work of detachment W_{adh} (nN × μm)	1.68	1.1	3.53	2.03	4.17	1.7
Young's modulus E_{cell} (Pa)	394	284	528	337	438	256
Characteristic distance δ(μm)	1.96	1.02	2.18	1.27	2.58	1.14
Global loading rate r_f(pN/s)	1.42×10^3	1.13×10^3	5.02×10^3	3.19×10^3	1.02×10^4	5.81×10^3

Figure 3 | Force-loading rate relationship at the global cellular level

The relationship between the maximal detachment force (F^* in pN) and the global loading rate (r_f in pN/s) plotted on a natural logarithmic scale and calculated as indicated in the text. The slope of the linear regression obtained on many cells (one measure per cell) gives the reference force F_β and the linear regression intercept with vertical axis at $r_f = 1$ pN/s provides the natural dissociation rate K^0_{off} (in s^{-1}) using the relation $[F^*]_{r_f=1pN/s} = -F_\beta \ln(K^0_{off} F_\beta)$.

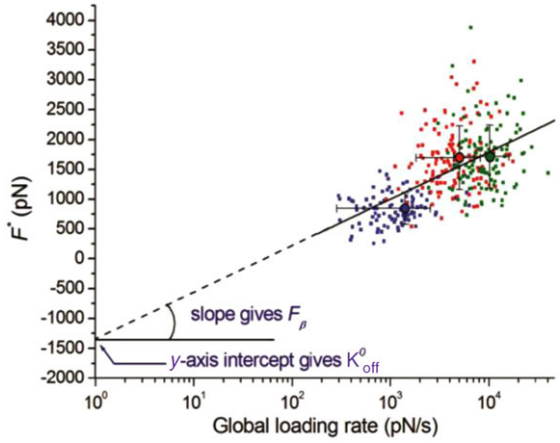

We also conducted a detailed analysis of the local rupture events on each cell-specific force–distance curve every time measurable rupture events could be identified (see *Material and Methods*). In general, several rupture events could be detected on each curve, leading to a larger number of local rupture events than the number of curves (n = 326–459; see Figure 4). Results are expressed in terms of local rupture force noted f^* for the different separation speeds. They are plotted in Figure 4 and summarised in Table 2. The magnitude of f^* is always much smaller than F^* (see Tables 1 and 2). For each separation speed, statistics of rupture forces follow a Gaussian distribution which is validated by the p values of the Kolmogorov–Smirnov (KS) test ($p \leq 0.01$) and confirmed by the Gaussian fit of histograms shown in Figure 4A. Significant differences are observed between the mean values of f^* measured for the three different separation speeds tested. To obtain the local loading rate preceding each rupture event, we measure the slope of the force–distance curve, right before the instant of bond rupture. The pre-rupture loading rate is locally obtained as indicated in *Experimental Methods* section. A linear regression line can be found between the measured rupture force f^* and the pre-rupture loading rate r_f (Figure 5). The slope of the linear regression line leads to the reference force f_β(≈30 pN) and the intercept at $r_f = 1$ pN/s leads to the natural dissociation rate, k^0_{off}(= 0.65 s^{-1}). For the regression line (not shown) relating the most likely values of f^* and r_f obtained in each group, we find close values: f_β(≈40 pN) and k^0_{off}(≈1.3 s^{-1}) (see Table 3).

Discussion

Comparison of MFS data with literature and theory

Integrins are transmembrane mechanoreceptors linking the actin cytoskeleton to the ECM through molecular bonds which individually generate weak contacts resisting only several tens of picoNewtons before subsequent strengthening (Cluzel et al., 2005). In the

Table 2 | Mean values ±SD of local rupture forces f^* and the local loading rates r_f estimated at three different predetermined separation speeds: $v = 2, 5\ 10\ \mu$m/s

	$v = 2\ \mu$m/s ($n = 64$)		$v = 5\ \mu$m/s ($n = 79$)		$v = 10\ \mu$m/s ($n = 28$)	
	Mean	SD	Mean	SD	Mean	SD
Local rupture force f^* (pN)	59.1	35.8	77.3	35.4	114.6	40.6
Local stiffness $k_{local} = df/dx$ (pN/μm)	131.7	114.9	61.9	45.1	93.2	75.5
Local loading rate r_f (pN/s)	263.3	229.7	309.6	225.3	931.9	755.3

The local loading rates are calculated from the local stiffness k_{local} (the slope of the force–distance curve preceding each rupture event) from the expression: $r_f = k_{local} \times v$. 'n' is the number of tested cells. The totality of the 'n' force–distance curves analysed in Table 1 for global parameters did not exhibit identifiable local rupture events, hence the smaller number 'n' of cells available for local rupture event analysis.

present study, integrins are probed in alveolar epithelial (A549) cells for short contact times (*i.e.* 2s) by MFS, leading to values of rupture forces for local rupture events in the range 60–115 pN. The short contact time corresponds to the initiation of adhesion reinforcement which is presumed to take place over the first minute, according to Taubenberger et al. (2007). In this phase of adhesion initiation, integrins start clustering but these receptors clusters remain small and are not necessarily detectable by conventional optical techniques (Laukaitis et al., 2001). Hence, the idea of the present study which consists in using a specifically defined MFS method to characterise this early phase of adhesion reinforcement. Noteworthy, the range of rupture forces presently found by MFS for local rupture events (60–115 pN) is inagreement with the range of force values (40–100 pN) found with a method called single-integrin unbinding rupture events (referred as DFS for dynamic force spectroscopy) by Taubenberger et al. (2007). The experimental conditions of Taubenberger et al.'s study and of the present study are very similar: contact times are much smaller than 1 min (*i.e.* 50 ms and 2 s, respectively), effective loading rates lie in a low range (*i.e.* $<10^4$ pN/s and $<10^3$ pN/s, respectively), whereas the integrin tested by Taubenberger et al. (*i.e.* $\alpha_2\beta_1$) in Chinese hamster ovary cells are also present in A549 cells. This similarity comforts the assumption that present local rupture events reflect the rupture of single integrin.

The early phase of integrin association is a critical step of cellular adhesion since formation of the first few bonds within short contact durations (seconds) results in a bond configuration with multiple-bond

Figure 4 | Histograms and statistics of local rupture forces f* for the three different speeds tested

(**A**) Histograms and (**B**) plotted values and box-whisker of the measured local rupture forces (f^* in pN) obtained from the force-step increases occurring on the force–distance curves. These two representations are given for three different predetermined separation speeds, namely v = 2 μm/s (blue diamonds); 5 μm/s (red diamonds); 10 μm/s (green diamonds). The squares in each rectangular boxes mark the mean value, whisker bars the ±SD values, and the horizontal lines in each box gives the median value. Black horizontal bars display statistical significance ($p < 0.001$). Note that the number of rupture events is much larger than the number of tested cells because of several rupture events per cell.

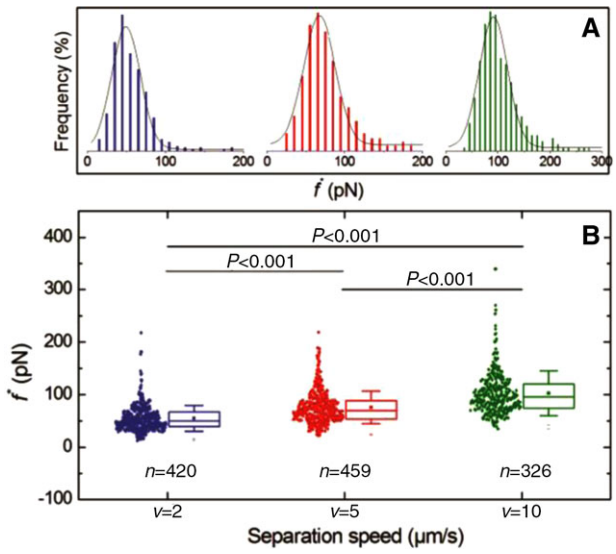

Figure 5 | Force-loading rate relationship at the local level Relationship between the local rupture force (f^* in pN) and the local loading rate (r_f in pN/s) plotted on a natural logarithmic scale and calculated as indicated in the text. The slope of the linear regression gives the reference force f_β and the intercept with vertical axis at $r_f = 1$ pN/s provides the natural dissociation rate k^0_{off} (in s^{-1}) through the relation $[f^*]_{r_f=1pN/s} = -f_\beta \ln(k^0_{off} f_\beta)$.

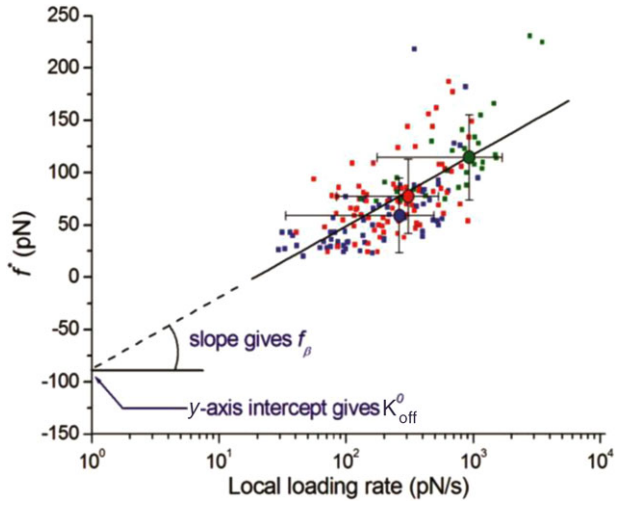

attachment supporting high mechanical strength, *i.e.* in the range from 1 to hundreds nanoNewton as typically found in a variety of membrane adhesion receptors (Bongrand and Bell, 1984) and notably for integrin–ligand interactions (Palecek et al., 1997). With the probing system presently used (see Material and Methods), we purposely aim at binding not one but several integrins. This leads to a reinforced bond strength because the force is exerted on a collective bond system. The efficiency of this collective bond association is verified by the level of detachment forces (*i.e.* range 1–2 nN) which is markedly above rupture forces presently found for the individual integrins (40–100 pN) composing the collective bond system. A similar conclusion was reached by Tautenberger et al. (2007) who similarly observed a reinforcement phase of rapidly increasing adhesion (preceding the maturation phase) except that we presently consider that the mechanism of reinforcement starts with non-cooperative bond association before cooperativity takes place in the process of adhesion maturation.

The theory of multiple bond association (see Materials and Methods and Williams, 2003) demonstrates that significant adhesion reinforcement is possible in non-cooperative bonds which remain dynamically independent, *i.e.* which break individually at random different times. Such adhesion situation occurs before cooperativity (Zhang and Moy, 2003) when independent bonds created at the probe–cell interface operate according to a 'parallel' bond configuration which uniformly distributes force amongst active bonds (Williams, 2003). We have previously shown in non-cooperative bonds that considerable increase in overall bond lifetime is brought by the homogeneous force distribution, whereas heterogeneous force distribution is not so efficient in terms of reinforcement (Isabey et al., 2013). The non-cooperative multiple bond model may also explain why measured strengths of a bond strongly depends on the pulling direction thus causing further variations in the unbinding force (Bustamante et al., 2004). Note that the parallel bond configuration is known to be appropriate during force spectroscopy measurements by AFM (Sulchek et al., 2005; Rankl et al., 2008). In the present study, we confirm experimentally and theoretically that the 'parallel' bond configuration is capable of inducing a rapid increase in rupture force by at least one order of magnitude.

Another consequence of the multiple bond parallel model concerns the calculation of the ratio between the slopes of the $F^* - \ln(r_f)$ and $f^* - \ln(r_f)$ linear relationships. This ratio provides a straightforward method to estimate the number of dynamically independent still non cooperative bonds. In present experiments, we obtain: $F_\beta / f_\beta = N f_\beta / f_\beta = N \approx 12$ (see Table 3). Although this estimate lacks accuracy because calculating a ratio doubles the error, the order of magnitude can be compared with previous studies. A substantially higher bond number was recently found (*i.e.* $N \approx 50 - 100$) for the same integrin-RGD binding during magnetic twisting cytometry (MTC) (Isabey *et al.*, 2016) which is consistent with the longer contact times used during MTC experiments (30 min) compared with AFM experiments (2 s). Direct comparison of F^* and f^* cannot be performed because these two quantities correspond to quite different loading rates. Nevertheless, one can compare the global and the local loading rates, and this comparison may lead to an alternative estimate of the bond number (see Material and Methods

Table 3 | Typical linear relationships obtained between force and loading rate obtained globally at the cell scale ($F^* - r_f$) (upper part of the table) and locally for each rupture event ($f^* - r_f$) (lower part of the table)

		Slope ($\approx F_\beta$) (pN)	Intercept (pN)	R	x_β (nm)	K^0_{off}(s^{-1})	T^0_{off} (s)
Global detachment force–global loading rate	Whole data set ($n = 332$)	342	-1.36×10^3	0.57	0.012	0.16	6.4
	Three-point method ($n = 3$)	467.4	-2.48×10^3	0.94	0.009	0.43	2.34
		Slope ($\approx f_\beta$) (pN)	Intercept (pN)	R	x_β (nm)	k^0_{off} (s^{-1})	t^0_{off} (s)
Local rupture force–local loading rate	Whole data set ($n = 171$)	29.7	–88.1	0.69	0.138	0.65	1.53
	Three-point method ($n = 3$)	40.3	–160	0.98	0.102	1.32	0.76

Two methods are tested: (i) a method based on the law of large numbers (from the 'n' cell tested) in which each point represents a given set of values: force and loading rate, obtained in a given cell, (ii) a method in which each point represents the three sets of values obtained for the three indentation speeds tested: mean value (±SD) of force for each corresponding mean value (±SD) of loading rate. Because distributions of force amongst cells or local rupture events are almost Gaussian (see Figures 3 and 5), the second method is close to the classical approach in which the most probable value (corresponding to the peak of probability density distribution) is plotted as a function of loading rate. First three columns: slope (*i.e.* reference forces F_β for global and f_β for local rupture events), the intercept with the vertical force axis, and the correlation coefficient R. Last three columns: values of x_β(distance at which energy barrier is located), natural dissociation rate K^0_{off} at global scale and k^0_{off} at local scale, and lifetimes at global and local scales, *i.e.* $T^0_{off} = (K^0_{off})^{-1}$ and $t^0_{off} = (k^0_{off})^{-1}$. Note that the two methods ((i) and (ii)) tested lead to similar differences in terms of magnitude for adhesion parameters estimated at global and local scales.

and Rankl *et al.*, 2008), *i.e.* $N = [\bar{r}_f]_{global}/[\bar{r}_f]_{local} = 5546\ pNs^{-1}/502\ pNs^{-1} \approx 11$, a value actually very close from that obtained by the ratio $F_\beta/f_\beta (= 12)$.

Complementarily, the experimental values of natural dissociation rates given in Table 3 ($k^0_{off} = 0.65$ and $K^0_{off} = 0.16$) lead to a ratio: ($k^0_{off}/K^0_{off} \approx 4$), which differs from the bond number given by the ratio: $F_\beta/f_\beta = N\ (= 12)$. This result is consistent with the prediction of the parallel bond model which would predict: $k^0_{off}/K^0_{off} \approx \ln N = 2.5$ for $N = 12$ (see Materials and Methods).

Linear force ramping appears to provide a satisfactorily curve-fitting model for the global and local bond rupture behaviours (see Figures 3 and 5) thus confirming the interest of the approach proposed (the so-called MFS method) to relate the global to local rupture events. Advantageously, the intrinsic biological variability is taken into account by performing measures in a large number of cells whereas minimising the force-induced cellular adaptation response by performing a unique force spectroscopy curve per cell. Biological variability is illustrated by the large values of standard errors found for global and local rupture forces as well as for loading rates (see Figures 3 and 5 and Tables 1 and 2). Indeed, we could not perform several measures of rupture force (global or local) at the same loading rate and thus could not make the statistics of rupture force (global or local) at predetermined loading rate because of biological variability. However, the relationships between rupture force and loading rates could be characterised (at global and local scales) by performing a wide number of rupture force measurements at various loading rates. Noteworthy, based on probability theory, the relationships obtained from a large number of trials should be close from the expected linear relationships predicted by the probability theory of single or multiple bond rupture (see Materials and Methods).

Cell elasticity characterisation by indentation

There is a close relation between cell mechanics and cytoskeleton (Li et al., 2008). This is particularly the case in the present study where the AFM probe is functionalised to be specific of transmembrane

integrins and beyond to the F-actin structure which is physically connected (Choquet et al., 1997). Nevertheless, for a small indentation, even in the absence of probe coating like in the study by Li et al. (2008), the cytoskeletal structure just beneath the cell surface membrane forms the region of interest. Note also that stress or strain adaptation response of the cell is avoided in the present study because a unique force–distance curve is performed for each given cell. Finally, although assumptions like homogeneous, isotropic, elastic material cannot be completely fulfilled when applying Hertz model, it is widely accepted that this model gives a good approximation of Young's modulus when the tests are conducted under small compressing or stretching deformations, *e.g.* presently ≤10% (Kuznetsova et al., 2007; Li et al., 2008). Young's modulus values presently obtained in A549 (range: 400–530 Pa) are in agreement with what is found by Li et al. (2008) in benign human breast epithelial cells using polystyrene beads of similar micrometer size (4.5 μm): similar range of curve fitting indentation depth (≤0.5 μm), a similar central location in the cell and the bottom range of loading rate (*i.e.* 0.03 Hz corresponding to a loading rate of 200 pN × 0.03 Hz ≈ 6 pN/s). Note that no loading rate dependence of Young's modulus was found in Li et al., as found in the present study. Moreover, in both studies, a spherical bead indenter is used instead of a sharp tip in order to get better assessment of cell elasticity by averaging over a larger cell surface area, while keeping contact geometry self-similar during indentation (Mahaffy et al., 2004). Finally, spherical bead are purposely used to minimise local strains and reduce the possibility of nonlinear or destructive cellular deformation (Dimitriadis et al., 2002).

Characterisation of the loading rate dependence of adhesion by MFS

The use of three separation speeds in the range 2–10 μm/s has permitted to extend over about two decades (but no more) the range of local and global loading rates, *i.e.* 30–3000 pN/s for the local loading rate (Figure 5) and 300–30,000 pN/s for the global loading rate (Figure 3). Regarding the wide number of AFM studies performed on single-molecule experiments in a variety of protein–ligand complexes – extensively reviewed in Lee et al. (2007) – local loading rates presently tested lie in the bottom range of the loading rates used in the single-bond literature. Moreover, the effective bond length or bond stretching distance is generally ≤1 nm which is presently the case for our local integrin–ligand bonds ($x_\beta = 0.138$nm) (see Table 3). In many cases, the force-induced dissociation of a ligand–receptor complex involves overcoming multiple activation energy barriers. For instance, in the streptavidin–biotin molecular complex which is a non-covalent single bond binding with one of the highest affinity levels, not one but several energy barriers were found (Grubmüller *et al.*, 1996; Evans, 2001; Pincet and Husson, 2005; Teulon *et al.*, 2011). The energy landscape of single-molecule integrin–ligand bonds is most likely different because the integrin binding force lies in a much smaller range than the one of the streptavidin–biotin molecular complex (*i.e.* 32–97 pN for integrins linked to different RGD-ligands in (Lehenkari and Horton, 1999) and up to 200–300 pN for streptavidin–biotin in Evans (1998). Using a wide range of loading rates (r_f: $10^2 \rightarrow 10^5$ pN/s), Zhang et al. (2004) found at least two activation potential energy barriers (a steep inner barrier and a more elevated outer barrier) for the integrin $\alpha_4\beta_1$–vascular cell adhesion molecule-1 (VCAM-1) interactions. In the case where the system must overcome a series of increasingly higher energy barriers before final dissociation (*i.e.* possibly different from the presently studied integrin system), the dissociation kinetics of the complex at low loading rates is governed by the properties of the outmost barrier (Li et al., 2003). In the present study, because the loading rate is limited to the low range, data for rupture force and loading rate dependence (shown in Figures 4 and 5) reflect the external energy barrier and not the inner one if any. This is why a unique linear curve fitting was found sufficient to provide a satisfactorily adjustment while a fitting of rupture forces on a larger range of loading rate might have required double slope adjustment to include the inner barrier behaviour (Lee et al., 2007). Similarly, the force spectra (or histograms) obtained for different separation speeds (still leading to explore the low range of loading rates) (Figure 4) reflect the dynamic strength (rupture forces) of the outermost energy barrier while the innermost barriers are not presently accessible with such a low range of loading rates (Evans and Ritchie, 1997). The statistics of local events shown in Figure 4A and Table 2 provides values of rupture forces consistent with this

assumption. Because the present study is limited to short contact times (presently a couple of seconds), the activation of adhesion state is limited (Taubenberger et al., 2007) and the outer barrier which is the site of integrin activation not affected (Li et al., 2003). Moreover, force spectroscopy manoeuvers are performed only once in a given cell in order to minimise cellular stress/strain adaptations, meaning that present results could not be affected by preliminary integrin activation. Another critical aspect recently discovered in single molecule bonds (essentially the streptavidin–biotin interaction) and stretched by a combination of force ramp or force clamp concerns the dependence of dissociation rate on the force history as well as on the instantaneous force applications (Marshall et al., 2005; Pincet and Husson, 2005). Note however that these history and force dependent features failed to be observed in bonds involving the β_2-integrin (Evans et al., 2010).

In other words, present experimental conditions are chosen in order to simplify a multibond system which is necessarily complex: only the outer energy barrier is considered (see above), only the early response of attachement is considered (contact time 2 s) but the set-up permits multiple bond attachments. Moreover, force upon contact must be small but not too small (5 nN) to permit multiple binding. As a result, the histograms of rupture forces presently obtained from the local rupture events statistically follow a Gaussian distribution (see Figure 4A). Using similar experimental conditions, Taubenberger et al. (2007) found that at early steps, $\alpha_2\beta_1$ integrin–collagen rupture forces also follow Gaussian distribution with satisfactorily statistical significance. In most cases, the rupture forces showed Gaussian distribution (KS test; $p \leq 0.01$), indicating that a single class of unbinding events was detected (Evans and Ritchie, 1997). As mentioned in a previous study (Kinoshita *et al.*, 2010), by limiting the duration of contact, one can establish uniform conditions under which attachments are formed at every touch, allowing the rare events to be characterised by Poisson statistics – Gaussian distribution being a limiting form of the Poisson distribution. At the same time, histograms reflecting the statistics of single bond integrin-RGD behaviour (outer barrier only and short contact times), a Gaussian distribution is likely to provide a satisfactorily fitting of force rupture histograms, thus confirming the above assumption that 'individual' rupture events reflect single bond behaviour in the experimental conditions and for the receptor–ligand bond system presently tested.

Integrin linkages in A549 cells

Integrins are heterodimeric transmembrane receptor proteins that mediate cell–cell and cell–ECM interactions (Hynes, 2002) often via the specific RGD motif which is presently used to coat the beads. The specificity of RGD-binding integrins include five integrin subunits α_V ($\alpha_V\beta_1$, $\alpha_V\beta_3$, $\alpha_V\beta_5$, $\alpha_V\beta_6$ and $\alpha_V\beta_8$), two β_1 integrin subunits ($\alpha_5\beta_1$ and $\alpha_8\beta_1$) and $\alpha_{IIb}\beta_3$ (Humphries et al., 2006). Integrin subunits expressed at the apical surface of A549 cells are, by decreasing order of importance: $\beta_1, \alpha_3, \alpha_6, \alpha_5$ and α_2 (Massin *et al.*, 2004). In addition, integrin subunits α_V associated with integrin subunits β_3 and β_6 are expressed in A549 cells (Merilahti et al., 2016). Incidentally, the forces measured for individual bond rupture in Fibronectin–$\alpha_5\beta_1$ interactions lie in the range of rupture forces presently found in our cellular model: 39 ± 8 pN in (Li et al., 2003) and 40–100 pN for (Sun et al., 2005).

The specificity of bead RGD coating guarantees the specificity of integrin linkage. Indeed, without coating (case of plasma treatment) or with a non-specific integrin coating like BSA force spectroscopy measurements lead (in Figure 1) to significantly smaller detachment forces F^* compared with a specific RGD-coating which moreover minimises non-specific bonds by plasma treatment. In addition to this adhesion specificity, the use of short contact times (2 s) to prevent switching to a fully activated adhesion state (Taubenberger et al., 2007) as well as the use of a unique force spectroscopy curve per cell to prevent force history effects (Marshall et al., 2005) tend to justify one of the model assumptions in which all bonds have identical energy barriers, *i.e.* a similar maturation adhesion state (see Materials and Methods). Another important assumption of the model is that long cellular extensions performed during force spectroscopy experiments (presently up to 25 μm; see Figure 6C) prevents close coupling between bonds, meaning that uncorrelated failure mode and absence of rebinding are two reasonable assumptions for our model. Both assumptions have been used in previous multiple bond studies (Sulchek et al., 2005; Rankl

Figure 6 | See Legend on next page

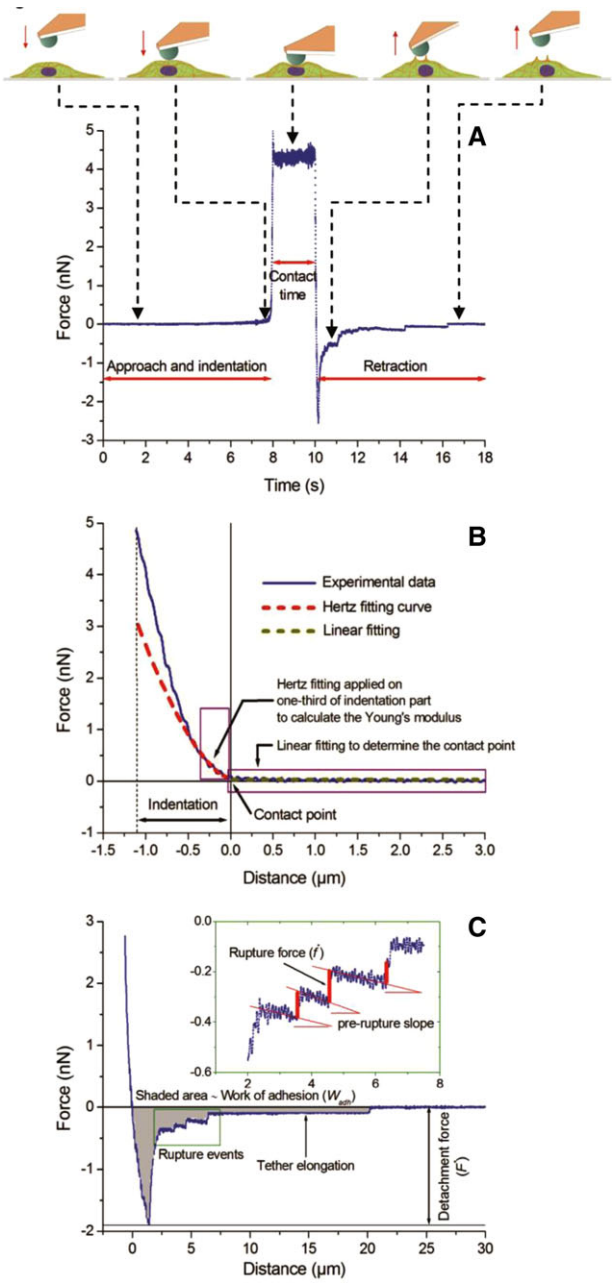

Figure 6 | Strategy for measuring adhesion parameters by the Multiple bond Force Spectroscopy (MFS) approach using AFM

(**A**) Typical force–time-dependent signal obtained by AFM device showing the sequence of successive manoeuvres used for cellular experiments. Three characteristic periods can be observed: (i) Approach and indentation of a RGD-coated spherical probe (diameter: 6.6 μm) at predetermined constant speed (5 μm/s on this record) up to the maximal pressing force of about 5 nN, (ii) Cell contact during 2 s at contact force of 5 nN, (iii) retraction curve obtained at the same predetermined constant speed (*e.g.* 5 μm/s). (**B**) Typical force–distance curve (blue curve) in the approach and indentation periods used to calculate cell rigidity on a given cell (Young's modulus in Pa) obtained by the Hertz model (red dash line) fitted on the initial portion (≈30%) of the cell indentation applied from the contact point determined by the intercept between the Hertz model (red dash line) and the horizontal linear fitting (green dash line). (**C**) Typical force–distance curve (blue curve) in the retraction period showing how global and local adhesion parameters are obtained in a given cell: (i) the maximal detachment force in nN range (or global rupture force: F^* which is the highest negative force value recorded and the work of adhesion W_{adh} in nN × μm calculated from the shaded area, (ii) the local rupture events (step increase) which aim at characterising (see insert) the single bond rupture forces (in pN range) and the local cellular/molecular stiffness (k_{local}) from the negative slopes preceding local bond ruptures. In case of zero slope (plateau) which is attributed to tether extension with no measurable cell stiffness, the local loading rate could not be estimated and the rupture force data did not enter in the statistics of the loading rate dependence of rupture force.

et al., 2008). Compared with integrins at the bead–cell interface, integrins on basal face of culture of A549 cells are arranged into higher organised structures, such as focal complexes, focal adhesions and fibrillar adhesions (Geiger and Bershadsky, 2001). In these mature adhesive contacts, integrins are linked to the tensed cytoskeleton via their intracellular domains and through a multitude of structural adapter proteins, such as vinculin, talin and α-actinin and signalling adapter proteins, such as paxillin, src, cas and FAK (Zamir and Geiger, 2001). Collectively, these receptors contribute to high mechanical strength attachments typically having hundreds of nanoNewtons which is far beyond the levels of adhesion reinforcement presently found for the early phase of adhesion (a few nN only). Indeed, whereas the molecular composition of integrin complexes and the signalling pathways controlling their macroscopic assembly or disassembly have been analysed in detail, less is known about the early molecular events leading to the early critical phase of integrin-based adhesion reinforcement.

Conclusions

The mechanisms of early adhesion reinforcement is very general and needs to be tested in experiments in which bonds are uniformly stretched because such parallel bond configuration theoretically enables high efficiency in terms of adhesion reinforcement (Isabey et al., 2013). Parallel configurations are difficult to evaluate experimentally without a specific set up. AFM experiments enable stretching bonds in such configuration by contrast to other techniques (*e.g.* flow chamber, MTC), in which bonds are non-uniformly stretched. Williams (2003) has shown that the force-induced rupture of multiple uncorrelated bonds can be described by a Markovian sequence enabling to predict the increase in rupture force resulting from bond association. Our approach is similar (see Materials and Methods) except that the use of analytical expressions of the unbinding dissociation rates (Isabey et al., 2013) allowed us to show that a Bell-type model can be used for parallel and zipper bond configurations, leading to explicit expressions of rupture force in terms of number of bonds N and the effective loading rate r_f. To validate our multibond model, we use MFS, a method which allows to relate a 'global' rupture event to 'local' rupture events in a given force spectroscopy curve. The statistics of global and local rupture forces was performed by plotting, for a large number of trials, the relationships between rupture forces and effective loading rates for global (multiple bonds) and local (single bond). The linear relationships found are indeed predicted by the probability theory of single or multiple bond rupture and permit to determine the number of non-cooperative integrin receptors involved in the multiple bond response. By contrast, previous studies on the early steps of integrin binding (Taubenberger et al., 2007) were not able to determine the exact number of integrin receptors per adhesive unit. Moreover, the single-bond DFS experiments used in previous approaches require a very low frequency of successful binding events to avoid multiple attachments. This makes single-bond experiments time consuming and the accumulation of rupture force histograms difficult (Erdmann et al., 2008). AFM has the great advantage of generating a speed-controlled unidirectional stretching between a purposely functionalised probe and integrin mechanoreceptors. In contrast to previous force spectroscopy studies in which a narrow sharp indenter was used (Lehenkari and Horton, 1999; Lee and Marchant, 2001), the spherical shape and the micrometric size of the probe was chosen in order to create not a unique, but several CSK-specific bonds working together while inducing minimal depth of cell indentation.

Material and methods

Theoretical methods and applications

Theory of multiple bond rupture

Cell adhesion is mediated by highly specific, weak receptor ligand bonds (Bell, 1978; Evans and Calderwood, 2007; Erdmann et al., 2008) which must work together to sustain forces (Evans, 2001). We recently demonstrated that multiple bonds, working stochastically, *i.e.* breaking non-simultaneously, have extended lifetime. This means that associating dynamically independent bonds (previously called uncooperative bonds (Williams, 2003)) results in adhesion stabilisation and thus adhesion reinforcement (Isabey et al., 2013). However, the efficiency of this stabilisation critically depends on bond number as well as on the failure mode. The latter is characterised by the way the force is distributed amongst the bonds, homogeneously or not. This leads us to consider two opposed bond configurations: 'parallel' and 'zipper'. In the parallel configuration, the force applied on the collective bond structure is homogeneously redistributed amongst the existing bonds each time a bond breaks stochastically. In the zipper configuration, the force distribution is totally heterogeneous, the totality of the force being applied on the leading bond. After random rupture of the leading bond, the neighbouring bond then receives the totality of the force, and so on until complete bond rupture. The stabilisation mechanism resulting from bond association enables adhesion reinforcement, but depending on bond configuration, fundamental differences appear in the force-dependent dissociation rate and in the rupture force of the global bond system. We detail below a theoretical approach describing the effect of bond number on the global rupture force for each configuration, knowing that the consequences on global bond lifetimes have already been described in a previous paper (Isabey *et al.*, 2013).

The multiple bond rupture approach

The Kramer-Smoluchowski theory predicts that the global lifetime needed to transit across n sharp energy barriers – not necessarily of identical magnitude – is the sum of the times needed to transit across each individual energy barrier (Evans, 1998,2001). The inverse of the lifetime is the dissociation rate, $K_{\text{off}}(f)$, whose expression is thus given by:

$$K_{\text{off}}\left(f\right) = \frac{1}{T_{\text{off}}(f)} = \frac{1}{\sum_{n=1}^{N}\left(t_{\text{off}}^{0}(n)\exp\left(-\frac{f}{f_{\beta}(n)}\right)\right)} \quad (1)$$

where f is the force applied on the associated bond structure and $t_{\text{off}}^{0}(n)$ is the typical crossing time of the n^{th} barrier. This time exponentially depends on the height of the chemical energy barrier above the bound state. $f_{\beta}(n)$ is the force scale of each individual energy barrier classically defined by:

$$f_{\beta}(n) = \frac{k_{\text{B}}T}{x_{\beta}\,(n)} \quad (2)$$

k_BT is the thermal energy scale (= 4.11 pN × nm) and $x_\beta(n)$ is the bond stretching distance in the direction of the force at which the energy barrier is located (called transition state). Studying the force–response of collective bonds made of N identical energy barriers (*e.g.* integrin–ligand), for fully homogeneous (parallel bond configuration) or fully heterogeneous (zipper bond configuration) force distributions, we recently demonstrated (Isabey et al., 2016) that Eq. (1) can be approximated by a Bell-type model whose prefactor and exponent depend on the failure mode (or bond configuration) as indicated hereafter:

$$K_{off}(f) = K_{off}^0 \exp\left(\frac{f}{F_\beta}\right) \tag{3}$$

where f is the total force of separation of the collective bond. The prefactor K_{off}^0 is the natural dissociation rate and the denominator of the exponent, F_β, is a reference force. Eq. (3) means that single and multiple bonds can be understood through the same mathematical description. Noteworthy, the parallel association results in a weak N-dependence of the natural dissociation rate, *i.e.* $K_{off}^0 \approx \frac{k_{off}^0}{\ln N}$, for $N > 10$ and $f \to 0$ or $K_{off}^0 \approx k_{off}^0\sqrt{2}\left(\frac{f}{Nf_\beta}\right)^{0.5}$ for $N \geq 2$ and $f \neq 0$. In addition, in the parallel bond configuration, the reference force is proportional to N, *i.e.* $F_\beta = Nf_\beta$. By contrast, the zipper configuration results in a stronger decrease in the natural dissociation rate, $K_{off}^0 = \frac{k_{off}^0}{N}$, whereas its reference force remains unchanged compared with the single bond: $F_\beta = f_\beta$. Assuming that the dynamics of multiple bonds alike single bonds can be described by a first-order Markov process through an overall or global time-dependent dissociation rate $K_{off}(t)$, the probability of bond survival $P(t)$ obeys to the following first-order differential equation in which rebinding is neglected during the force separation manoeuver ($K_{on}(t) = 0$):

$$\frac{dP(t)}{P(t)} = K_{off}(t)\,dt \tag{4}$$

The solution to Eq. (4) takes the following typical form (Evans and Kinoshita, 2007):

$$P(t) = \exp\left[-\int_0^t K_{off}\left(f\left(t'\right)\right)dt'\right] \tag{5}$$

Derivation of the collective bond rupture forces

As for single bonds (Evans and Kinoshita, 2007), applying a force ramp, $r_f = df/dt = cste$, on all bonds enables to quantify the profile of dissociation kinetics with force. The most likely rupture force F^*corresponding to vanishing probability density $p(f)$ can thereby be determined: $[p(f)]_{f=F^*} = \left[\frac{\partial P(f)}{\partial f}\right]_{f=F^*} = 0$.

F^* satisfies the condition:

$$\left[\frac{K_{off}(f)}{r_f}\right]_{f=F^*} = \left[\frac{\partial\left(\ln\left(K_{off}(f)\right)\right)}{\partial f} - \frac{\partial(\ln(r_f))}{\partial f}\right]_{f=F^*} \tag{6}$$

Taking $\partial(\ln(r_f))/\partial f \approx 0$ (because the loading rate is assumed to be constant), and using the expression of $K_{off}(f)$ given by Eq. (3), leads to: $[K_{off}^0 \exp(f/F_\beta)]_{f=f^*} = r_f/F_\beta$. From this equation, the most probable rupture force of the collective bond assembly F^*can be obtained:

$$F^* \approx F_\beta \ln\left[\frac{r_f}{K_{off}^0 F_\beta}\right] \tag{7}$$

This equation justifies that the values of the F_β can be experimentally obtained from the slope of a linear regression (fitted using least square method, correlation coefficient R given in Table 3) on all points of the graph: $F^* - \ln(r_f)$, whereas the value of K_{off}^0 can be obtained from the intercept between this regression line and, *e.g.* the vertical axis ($[F^*]_{\ln r_f = 0} = -F_\beta \ln(K_{off}^0 F_\beta)$).

$K_{off}^0 F_\beta$ appears as a reference scale for the loading rate r_f. Noteworthy, r_f in Eq. (7) is the effective loading rate applied on the collective bond structure. Expression giving F^*(Eq. (7)) is similar to the classical rupture force expression given for single bond $f^* \approx f_\beta \ln\left[\frac{r_f}{k_{off}^0 f_\beta}\right]$ (Evans and Ritchie, 1997; Evans, 1998) except that the loading rate r_f is the actual loading rate preceding the single bond rupture. For parallel bond systems, the effective loading rate applied on each individual bond composing the collective bond, is divided by the number of active bonds, r_f/N, because force is redistributed among all remaining bonds at each rupture step (Rankl *et al.*, 2008). The consequence is that the treatment of loading rate cannot be the same for individual bonds and multiple bond structures as it should take into account the proper loading rate preceding the rupture event.

For the parallel bond configuration, the finding of an analytical expression for $K_{off}(f)$ (Eq. (3)) as proposed by Isabey et al. (2013) enables to calculate the global rupture F^* by the following expression:

$$F^* = F_\beta \ln\left[\frac{r_f}{K_{off}^0 F_\beta\left(\frac{2}{2+F_\beta/F^*}\right)}\right] \approx F_\beta \ln\left[\frac{r_f}{K_{off}^0 F_\beta}\right]$$
$$= Nf^* - \varepsilon N f_\beta \text{ with } \varepsilon < 1 \text{ and } N \geq 2 \tag{8}$$

Eq. (8) shows that the rupture force of multiple identical bonds associated in parallel is at first order proportional to the bond number through the linear N-dependence of $F_\beta = Nf_\beta$. F^* is also approximately proportional to the logarithm of the loading rate r_f and represents less than N times the rupture force of individual bonds composing the collective bond.

For a fully heterogeneous distribution of force on collective bonds (zipper configuration), the global rupture force F^*can be obtained from:

$$F^* = f_\beta \ln\left[\frac{r_f}{f_\beta k_{off}^0/N}\right], \; i.e.$$
$$F^* = f_\beta \ln\left[\frac{r_f}{f_\beta k_{off}^0}\right] + f_\beta \ln N = f^* + f_\beta \ln N \tag{9}$$

Eq. (9) shows that the N-dependence of the rupture force is weak. More precisely, the global rupture force is only increased by the quantity $f_\beta \ln(N)$ which varies only weakly with N. Incidentally, the logarithmic r_f-dependence of the rupture force predicted by Eq. (9) is similar for zipper and parallel bond configurations as already shown by Eq. (7). In other words, as N increases, the reinforcement permitted by the parallel bond

configuration is markedly higher than that the one permitted by the zipper configuration. This adhesion reinforcement can thereby be evaluated through a characterisation of bond number and bond configuration by comparing the $\ln(r_f)$-dependence of rupture forces (i) in a multiple bond system (F^*) and (ii) in the individual bonds f^* which properly constitute the multiple bond structure. This comparison can be performed by AFM throughout a given force spectroscopy curve to the extent that this curve contains – not one as in standard single bond force spectroscopy (Taubenberger *et al.*, 2007) – but several bond rupture events. This requires that a multiple bond system has been created between the AFM probe and the cell (Figure 6). Such a method called *MFS* is proposed and evaluated in the present study. AFM experiments are purposely conducted with a spherical probe of micrometer size (diameter 6.6 μm), and a contact force of 5 nN which generates a cellular indentation up to 1.5 μm, corresponding to a contact area with the cell surface of several tens μm^2. We verified that using a contact time of 2 s between the cell and this RGD-functionalised probe enables to generate several bonds whose characteristics in terms of bond number can be evaluated up to complete rupture by the MFS method presently proposed (Figure 6A).

Estimate of the effective loading rate

Based on Evans and Ritchie (Evans and Ritchie, 1997, 1999), the loading rate can be estimated from the product of the separation speed v (constant in AFM experiments) by the effective stiffness k_{eff}:

$$r_f = \frac{df}{dt} = \frac{df}{dx}\frac{dx}{dt} = k_{eff}\mathrm{v} \tag{10}$$

To enhance the variations in r_f, three predetermined separation speeds are imposed: v = 2, 5, 10 pN/s, while the variations in effective mechanical properties are measured but cannot be controlled. Estimating the effective stiffness k_{eff} is a critical step because this parameter account for the proper mechanical properties of the AFM cantilever on one side, and the cellular structure of the collective integrin-ligand bond (cell cortex, tensed actin filaments, etc.) on the other side. As in Odorico et al. (2007), we presently consider that the bond is connected at both ends to two deformable spring elements: the cantilever system whose stiffness is $k_{cant}(\approx 0.5$ N/m), and the cellular extension structure whose stiffness is k_{cell} which contributes to k_{cell}through: $k_{eff} = [\frac{1}{k_{cant}} + \frac{1}{k_{cell}}]^{-1}$. In the present experiments, $k_{cant} >> k_{cell}$ (leading to $k_{eff} \approx k_{cell}$ at global cell scale), hence $r_f = k_{cell}$v. Incidentally, spherical micrometer probes require higher indentation forces and thus stiffer cantilevers than sharp conical or pyramidal probes. These mechanical properties play a role in the kinetics properties of the bond(s) and have to be determined right before bond rupture both for single bonds and for collective bonds.

In present experiments, the cellular stiffness was determined at global and local scales:

i. At the global cellular scale, from the product of a characteristic cell deformation scale δ (deduced from the ratio between work of adhesion and maximum detachment force) and of the Young's modulus whose value is estimated, as explained below, at small deformation in the initial portion (*e.g.* one-third of the indentation distance: ≤ 0.5 μm) of the approach curve using the Hertz model (see Figure 6B). Note that at cell scale, this method appears more reliable than a method based on the measurement of a local derivative of the force–distance curve. Moreover, it has been shown that, at such low deformations, indentation and retract curves lead to similar values of Young's modulus (Bulychev et al., 1975).
ii. At the local cellular/molecular level by the slope of a straight line fitted through the final third of the retract force–displacement curve preceding the point of bond rupture (see enlargement in Figure 6C) as earlier proposed by several authors (Li et al., 2003; Taubenberger et al., 2007). This slope provides an estimate of the local cellular/molecular stiffness right before local rupture, $k_{local}(= df/dx)$. The local loading rate is obtained by $r_f(= k_{local}\mathrm{v})$, (Eq. (10)), assuming that the separation speed v is preserved throughout any of the local cellular extensions.

Determination of contact conditions and Young's modulus

The probe mounted on AFM cantilever is a bead of micrometer size (bead radius: = 3.3 μm) which is functionalised by a synthetic peptide RGD to be recognised by integrins. The spherical shape of the probe is chosen to avoid any membrane injury. With a maximum cellular depth of indentation h such that $h \leq 1.5$ μm (while cell height is around 6 μm), cellular deformations remain $\leq$25% and are systematically $<$10% (*i.e.* $h \leq 0.5$ μm) when calculating Young's Modulus with the Hertz model (see Figure 6B). With a contact force of 5 nN, the surface area of the bead–cell contact is ~ 30 μm^2 ($h = 1.5$ μm) which generates the formation of a certain number of 'kinematically independent' integrin-RGD bonds that the present approach aims at estimating.

In the 10% range of cellular deformation and in range of identical indentation and retraction speeds limited to 2–10 μm/s to guaranty quasi-static conditions and minimal hydrodynamic friction on the probe, vertical indentation force F is related to the indentation depth h by the Hertz model which enables to estimate the effective modulus of the probe–cell system E_{eff} (Kuznetsova et al., 2007):

$$F = \frac{4\sqrt{R}}{3} E_{eff} h^{3/2} \tag{11}$$

E_{eff} is calculated from (Kuznetsova et al., 2007):

$$\frac{1}{E_{eff}} = \frac{1-\nu_{probe}^2}{E_{probe}} + \frac{1-\nu_{cell}^2}{E_{cell}} \tag{12}$$

where E_{probe}, ν_{probe}, E_{cell}, ν_{cell} are the Young's modulus and the Poisson ratios for the probe material and the cell medium respectively. In practice, the probe is infinitely rigid compared with the cell, which leads to $E_{eff} \approx E_{cell}/(1-\nu_{cell}^2)$. Taking a Poisson ratio $\nu_{cell} = 0.5$ (Radmacher, 2002), Eq. (11) becomes:

$$F \approx \frac{16\sqrt{R}}{9} E_{cell} h^{3/2} \tag{13}$$

Young's modulus of cell E_{cell} can thereby be obtained from finding the E_{cell} value providing the best fit of Eq. (13) on the force-distance curve (see Figure 6B). As mentioned before, the probe with a spherical shape is supposed to generate lowest stresses and strains in comparison with the probes with other tip shapes (Dimitriadis *et al.*, 2002). Note that for $h \leq 0.5$ μm, the

substrate contribution can be neglected (Domke and Radmacher, 1998). In order to avoid a too large effect of intracellular spatial heterogeneities, cellular indentations were made systematically near the centre of the cell right and right above the nucleus. Moreover, to minimise the stress or strain-induced cell response to a cell indentation, force spectroscopy is performed from a unique indentation manoeuver per cell.

Experimental methods

Cell culture

The study is carried out on A549 cell line (ATCC) having a phenotype of human type II AEC. These cells express a wide variety of receptors and notably the transmembrane receptors of the integrin type (β_1, α_3, α_6, α_5 and α_2) (Massin et al., 2004). When forming a monolayer, A549 cells adopt a phenotype consistent with type II AECs *in vivo* and, importantly do not functionally differentiate in culture from type I AECs. They have the ability to form adherent and tight junctions when grown to confluence, and they offer many advantages for studying in vitro the pathophysiological response of AEC (Belete et al., 2010).

Several Integrin receptors bind the synthetic peptide containing the RGD sequence presents in many ECM components. The peptide RGD is classically used for integrin-specific cell-binding as done in the present study and in many previous studies (Féréol et al., 2008).

Cells were cultured in T25 flasks in DMEM-Glutamax High glucose medium (Gibco Life Technologies) supplemented with 10% foetal bovine serum (Sigma–Aldrich) under standard physiological conditions (37°C, 5% CO_2-95% air atmosphere, maximal humidity). Routine subcultures were made after 3–4 days once the confluence state, where cells cover more than 90% the surface, is reached. For sub-culturing in T25 flasks, a split ratio of 1/10 was used. For experiments, about 7×10^5 cells were extracted from the suspension and plated on petri-dish (TPP ϕ34 mm) coated with human fibronectin at a density of 10 ng/mm^2. The culture reached confluence in 24 h. Before experiments, cells were incubated for 30 min in serum free medium, CO_2-independent, supplemented with 0.5% BSA in order to block the non-specific binding (Planus et al., 1999).

AFM set-up

Force spectroscopy was conducted using commercial NanoWizard 1 AFM (JPK Instruments). The AFM is settled on the AxioObserver Z1 inversed microscope (Zeiss) which is placed on stabilisation table TL-150 (Table stable Ltd.). The microscope is equipped with a Zeiss EC-Plan-NEOFLUAR 20 × lens. Long-range force spectroscopy is made possible by the use of supplementary CellHesion module (JPK Instruments) comprising an electronic controller and a piezo-driven stage allowing a vertical displacement up to 100 μm. Measurements were carried out with a 6.6 μm-diameter spherical probe SquBe CP-CONT-SiO-C (Nanoandmore) mounted on a cantilever whose stiffness was around 0.5 N/m. The benefit of using such a micrometer spherical probe is that local strains, which may far exceed the linear regime, are minimised (Dimitriadis et al., 2002).

Probe preparation

AFM cantilever was washed with triton 0.5% for about 20 min then thoroughly rinsed with sterile water. Then, the probe was soaked in ethanol for 5 min and rinsed again in sterile water. Probe was left dry in biological safety cabinet. After that, probe underwent a plasma treatment (Harrick Plasma Cleaner-PDC-002-HPCE) in order not only to remove micro-organic contamination on probe surface, but also to make the surface hydrophilic and thus permeable to coating treatment. This preliminary plasma treatment is crucial because it enables the effective contact between the probe surface and the coating solution. In the absence of such treatment, we noticed that micrometric air bubbles prevent effective coating. The probe was sterilised under UV exposure for 25 min. Finally, the probe was dipped in 2.5 mg/ml RGD solution and stored at 4°C for 1 night. Before being mounted on the cantilever holder, the probe was thoroughly rinsed with PBS in order to eliminate unbound RGD peptides. The advantages of using cyclic RGD peptide instead of proteins are multiple: peptide generates no immune response, no infection risk, better stability, more simple orientation and single adhesion motif (Hersel et al., 2003).

Although the cantilever has a known nominative stiffness, it requires systematic calibration of its effective stiffness by the thermal noise oscillator method (Butt and Jaschke, 1995). According to the constructor, the recommended and presently used cantilever calibration procedure leads to an error smaller than 20%. This step was performed with a functionality fully integrated in the JPK interface. In our case, the cantilevers stiffness is around 0.5 N/m.

AFM measurements

First, a batch of cells is located out of the cell culture. In general, these cells must show the characteristic shape of adherent epithelium without any blebs, or damage. Cells, in ball shape or cells partly detached from the culture are not chosen. Second, by using 'Direct overlay' feature, a virtual coordination of respective optical image is created and stored in the AFM control unit memory so that the measurement points (cells) can be selected with precision. Measurements are performed on the cell membrane above the relatively flat nuclear region, *i.e.* where the cell thickness is always the highest and the contact geometry rather well defined. Once a batch is fully explored, the stage is moved towards another batch.

For each condition, about 40–60 cells were selected. Practically, instead of performing several measurements on each cell, our strategy was to get a unique force curve per cell. The advantages are many. First, we minimise the cell adaptation response to stress and notably cyclic adenosine monophosphate (cAMP) activation induced by the mechanical stimulation (Meyer et al., 2000; Tamada et al., 2004). Secondly, we favour intercellular variability instead of intracellular variability. Because AFM method enables to impose an unidirectional cell extension force from the beginning to the end of the stretching manoeuver, no change in bond configuration is likely is to occur in the course of separation.

A typical measurement cycle comprises 3 phases (see Figure 6A): (i) Approach: the piezo moves the stage upwards so that the cell is brought into contact and the probe deforms the cytoplasm until a point of maximum effort is reached, *i.e.* contact force = 5 nN, thereby providing an approach force curve; (ii) Contact: the stage is immobilised (constant height) during a predetermined contact time (set at 2 s). The force remains almost constant to enable adhesion in its early phase. These contact

conditions were chosen after preliminary experiments aiming at finding the best compromise between a sufficient number of rupture events and complete bond rupture during the retraction period; (iii) Retraction: at the end of the contact time, the piezo moves the stage downwards at the same constant speed, the probe is progressively separated from the cell and the bonds created at the extremity of cellular extensions break randomly thereby generating sudden changes in force throughout the retraction force-curve. The cantilever speed is kept constant at three predetermined values: v = 2, 5 and 10 μm/s. This speed range is purposely limited in order to minimise the duration of force spectroscopy (maximum half a minute per cell) and thus to avoid cell morphological changes. Closed-loop system is activated in order to precisely control the z-movement. The z-movement of 35 μm from contact point leads to the total separation of the probe from cells in most of presently studied cases. The sampling rate is set at 1 kHz allowing to capture rapid change in signal.

Data processing

Force curves analysis was performed with JPK data processing. We first created a procedure comprising a series of functions supplied by the software toolbox. These functions are: (i) curve smoothing to eliminate high frequency noise; (ii) force curve baseline correction for both the offset and tilt of the linear part on the right of force curve (far from the surface); (iii) contact point determination; (iv) calculation of the real tip-sample distance by correcting the bending of the cantilever; (v) lowest point determination on the retraction curve corresponding to the detachment force; (vi) calculation of area located between the retraction curve and x-axis corresponding to the work of adhesion; (vii) calculation of Young's modulus by curve fitting of the linear portion on the approach curve to determine the contact point and fitting one-third of indentation curve by the Hertz model. Batch processing is then enabled by applying the registered procedure to the whole force curves. During the processing, each curve is monitored. All curves showing abnormal shapes, such as wavy shape in the far-from-surface part or contact force higher than the preset value (5 nN), are excluded from the analysis. Only curves processed from the batch processing are further individually analysed to quantify the rupture forces. Due to the moderate range of approach and separation speeds used in this study (v = 2, 5, 10 μm/s), the hydrodrag is negligible for speeds of 2 and 5 μm/s and, is smaller than 10 pN for the speed of 10 μm/s, leading to an error less than 10% in measuring rupture forces which has presently been neglected.

The overall cellular adhesion between the cell and the probe is characterised by the maximal detachment force noted F^* and the work of adhesion noted W_{adh}. The probe size is such that the cell–probe contact area represents a typical cell–matrix adhesion site, *e.g.* focal adhesion site, with a certain number of integrins engaged. Hence F^* and W_{adh} are able to characterise to the collective response of multiple integrin bonds created between the cell and the bead surface. These parameters are obtained directly from the retraction curve (see Figure 6C): the maximal detachment force noted F^*corresponds to the highest negative values on each force–distance curve, *i.e.* the maximal attractive force that the multiple bond system created can sustain. The work of adhesion W_{adh} is a convolution of cell mechanics and cell adhesion energies needed to reach complete separation of the probe from the cell. This quantity corresponds to the integrated surface area delimited by the abscissa and retraction curve (see Figure 6C).

Local bond rupture events are also identified by analysing locally the transient increases in the retraction force–curve (Figure 6C). On these curves, we observe two typical rupture events: some local rupture events are preceded by a segment with constant negative slope, whereas some others (*i.e.* classically referred as tethers formed by plasma membrane) are preceded by a plateau. The first type of events originate from the cytoskeleton mechanical properties, *e.g.* the compliant properties of actin filaments (Friedrichs et al., 2013). So, measuring the negative slope provides an estimate of the actual mechanical system behind each bond, knowing that the bond response to mechanical loading, *e.g.* the rupture force, depends on these mechanical conditions through the loading rate. Since the present study deals with collective bond rupture whose theory has been described in the first paragraph of this chapter, it is worth doing the statistics of rupture forces with these local loading rate conditions. However, no force loading (increase in force) occurred for rupture events preceded by a force plateau. These events were interpreted as membrane tether extrusions from a large cell membrane reservoir (Evans and Calderwood, 2007). Because the force rupture analysis in this study required constant-rate, nonzero bond loading before rupture, values of rupture events preceded by a force plateau were excluded as done in Taubenberger et al. (2007). The information extracted from the local bond rupture events can then be compared with the one coming from more global rupture events, assessed through maximal detachment force and the work of adhesion. Note however that W_{adh} integrates the above mentioned different types of rupture events.

To characterise the relationships between F^* (respectively f^*) and the global (respectively the local) loading rates r_f, two methods of data analysis are used: (i) a linear regression performed on all data points, each point representing a couple of measured values: force and loading rate, (ii) a linear regression performed on the three mean values obtained after averaging data points obtained at each one of the three separation speeds tested (v = 2, 5 and 10 μm/s). This first method is based on the law of large numbers which states that because of large number of data points, the found relationship is close to the expected relationship predicted by the probability theory for single or multiple bond rupture. The second method is close to the classical approach (Eq. (7)) in which the most probable value (corresponding to the peak of probability density distribution) is dependent on the logarithm of the loading rate.

Statistical tests

All tests were performed using statistical software package Statistica v7.1 (StatSoft). We used non-parametric Kruskal–Wallis test for the comparison of the mean values and KS test for normality. A p value ≤ 0.05 was considered significant and $p \leq 0.001$ was highly significant.

Author contribution

N.-M.N. designed, performed the experiments, analysed data and wrote the paper; C.A. designed, performed experiments, analysed data and wrote the paper; S.A.D. provided assistance in cell experiments

and proofread the paper; E.P. provided expertise on cell biology and corrected the paper; M.F., G.P. and B.L. provided physical expertise, mathematical computation and corrected the paper and D.I. designed and coordinated the study and wrote the paper.

Funding

For this research, we acknowledge receipt of grants from Agence Nationale de la Recherche: ANR no 2010-BLAN-1119-05 and from Fondation pour la Recherche Médicale: FRM programme Bio-Ingénierie pour la Santé 2014, DBS 20140930771.

Conflict of interest statement

The authors have declared no conflict of interest.

References

Belete, H., Godin, L., Stroetz, R. and Hubmayr, R. (2010) Experimental models to study cell wounding and repair. Cell. Physiol. Biochem. **25**, 71–80

Bell, G. (1978) Models for the specific adhesion of cells to cells. Science **200**, 618–627

Bongrand, P. and Bell, G.I. (1984) Cell-cell adhesion: parameters and possible mechanism. In: A.S. Perelson, C. DeLisi and F.W. Wiegel (Eds.). *Cell Surface Dynamics. Concepts and Models.* New York: Marcel Dekker, pp. 459–493

Bulychev, S.I., Alekhin, V.P., Shorshorov, M.K., Ternovskii, A.P. and Shnyrev, G.D. (1975) Determining Young's modulus from the indentor penetration diagram. Zavod. Lab. **9**, 1137–1140

Bustamante, C., Chemla, Y.R., Forde, N.R. and Izhaky, D. (2004) Mechanical processes in biochemistry. Annu. Rev. Biochem. **73**, 705–748

Butt, H. and Jaschke, M. (1995) Calculation of thermal noise in atomic force microscopy. Nanotechnology **6**, 1–7

Cardinal, L.J. (2015) Central tendency and variability in biological systems. J. Community Hosp. Inter. Med. Perspect. **5**, 1–4

Choquet, D., Felsenfeld, D.P. and Sheetz, M.P. (1997) Extracellular matrix rigidity causes strengthening of integrin-cytoskeleton linkages. Cell **88**, 39–48

Cluzel, C., Saltel, F., Lussi, J., Paulhe, F., Imhof, B.A. and Wehrle-Haller, B. (2005) The mechanisms and dynamics of $\alpha v\beta 3$ integrin clustering in living cells. J. Cell Biol. **171**, 383–392

Dimitriadis, E.K., Horkay, F., Maresca, J., Kachar, B. and Chadwick, R.S. (2002) Determination of elastic moduli of thin layers of soft material using the atomic force microscope. Biophys. J. Elsevier. **82**, 2798–2810

Discher, D., Janmey, P. and Wang, Y. (2005) Tissue cells feel and respond to the stiffness of their substrate. Science **310**(November), 1139–1143

Domke, J. and Radmacher, M. (1998) Measuring the elastic properties of thin polymer films with the atomic force microscope. Langmuir **14**, 3320–3325

Erdmann, T., Pierrat, S., Nassoy, P. and Schwarz, U. (2008) Dynamic force spectroscopy on multiple bonds: Experiments and model. Europhys. Lett. **81**, 48001-p1-p6

Evans, E. (1998) Energy landscapes of biomolecular adhesion and receptor anchoring at interfaces explored with dynamic force spectroscopy. Farad. Discuss., **111**, 1–16

Evans, E. (2001) Probing the relation between force—lifetime—and chemistry in single molecular bonds. Annu. Rev. Biophys. Biomol. Struct. **30**, 105–128

Evans, E.A. and Calderwood, D.A. (2007) Forces and bond dynamics in cell adhesion. Science **316**(May), 1148–1154

Evans, E. and Kinoshita, K. (2007) Using force to probe single-molecule receptor-cytoskeletal anchoring beneath the surface of a living cell. Methods Cell Biol. **83**, 373–396

Evans, E., Kinoshita, K., Simon, S. and Leung, A. (2010) Long-lived, high-strength states of ICAM-1 bonds to beta2 integrin, I: Lifetimes of bonds to recombinant alphaL beta2 under force. Biophys. J. **98**, 1458–1466

Evans, E. and Ritchie, K. (1997) Dynamic strength of molecular adhesion bonds. Biophys. J. **72**, 1541–1555

Evans, E. and Ritchie, K. (1999) Strength of a Weak bond connecting flexible polymer chains. Biophys. J. **76**, 2439–2447

Féréol, S., Fodil, R., Laurent, V.M., Balland, M., Louis, B., Pelle, G., Hénon, S., Planus, E. and Isabey, D. (2009) Prestress and adhesion site dynamics control cell sensitivity to extracellular stiffness. Biophys. J. **96**, 2009–2022

Féréol, S., Fodil, R., Pelle, G., Louis, B. and Isabey, D. (2008) Cell mechanics of alveolar epithelial cells (AECs) and macrophages (AMs). Respir. Physiol. Neurobiol. **163**, 3–16

Friedrichs, J., Legate, K.R., Schubert, R., Bharadwaj, M., Werner, C., Müller, D.J. and Benoit, M. (2013) A practical guide to quantify cell adhesion using single-cell force spectroscopy. Methods **60**, 169–178

Geiger, B. and Bershadsky, A. (2001) Assembly and mechanosensory function of focal contacts. Curr. Opin. Cell Biol. **13**, 584–592

Grubmüller, H., Heymann, B. and Tavan, P. (1996) Ligand binding: Molecular mechanics calculation of the streptavidin-biotin rupture force. Science **271**, 997–999

Hersel, U., Dahmen, C. and Kessler, H. (2003) RGD modified polymers: Biomaterials for stimulated cell adhesion and beyond. Biomaterials **24**, 4385–4415

Humphries, J.D., Byron, A. and Humphries, M.J. (2006) Integrin ligands at a glance. J. Cell Sci. **119**, 3901–3903

Hynes, R.O. (2002) Integrins: Bidirectional, allosteric signaling machines. Cell **110**, 673–687

Ingber, D.E. (2003) Mechanobiology and diseases of mechanotransduction. Ann. Med. **35**, 564–577

Isabey, D., Féréol, S., Caluch, A., Fodil, R., Louis, B. and Pelle, G. (2013) Force distribution on multiple bonds controls the kinetics of adhesion in stretched cells. J. Biomech. **46**, 307–313

Isabey, D., Pelle, G., André Dias, S., Bottier, M., Nguyen, N.M., Filoche, M. and Louis, B. (2016) Multiscale evaluation of cellular adhesion alteration and cytoskeleton remodeling by magnetic bead twisting. Biomech. Model. Mechanobiol. **15**, 947–963

Kinoshita, K., Leung, A., Simon, S. and Evans, E. (2010) Long-lived, high-strength states of ICAM-1 bonds to beta2 integrin, II: Lifetimes of LFA-1 bonds under force in leukocyte signaling. Biophys. J. **98**, 1467–1475

Kuznetsova, T.G., Starodubtseva, M.N., Yegorenkov, N. I., Chizhik, S. A. and Zhdanov, R. I. (2007) Atomic force microscopy probing of cell elasticity. Micron **38**, 824–833

LaCroix, A.S., Rothenberg, K.E. and Hoffman, B.D. (2015) Molecular-scale tools for studying mechanotransduction. Annu. Rev. Biomed. Eng. **17**, 12.1–12.30

Laukaitis, C.M., Webb, D.J., Donais, K. and Horwitz, A.F. (2001) Differential dynamics of alpha5 integrin, paxillin, and alpha-actinin during formation and disassembly of adhesions in migrating cells. J. Cell. Biol. **153**, 1427–1440

Lee, C.-K., Wang, Y.-M., Huang, L.-S. and Lin, S. (2007) Atomic force microscopy: Determination of unbinding force, off rate and energy barrier for protein-ligand interaction. Micron **38**, 446–461

Lee, I. and Marchant, R. (2001) Force measurements on the molecular interactions between ligand (RGD) and human platelet α IIb β 3 receptor system. Surf. Sci. **491**, 433–443

Lehenkari, P.P. and Horton, M.A. (1999) Single integrin molecule adhesion forces in intact cells measured by atomic force microscopy. Biochem. Biophys. Res. Commun. **259**, 645–650

Li, F., Redick, S.D., Erickson, H.P. and Moy, V.T. (2003) Force measurements of the alpha5beta1 integrin-fibronectin interaction. Biophys. J. **84**, 1252–1262

Li, Q.S., Lee, G.Y.H., Ong, C.N. and Lim, C.T. (2008) AFM indentation study of breast cancer cells. Biochem. Biophys. Res. Commun. **374**, 609–613

Liu, S., Calderwood, D.A. and Ginsberg, M.H. (2000) Integrin cytoplasmic domain-binding proteins. J. Cell Sci. **113**, 3563–3571

Mahaffy, R., Park, S., Gerde, E., Kas, J. and Shih, C. (2004) Quantitative analysis of the viscoelastic properties of thin regions of fibroblasts using atomic force microscopy. Biophys. J. **86**(3), 1777–1793

Marshall, B.T., Sarangapani, K.K., Lou, J., McEver, R.P. and Zhu, C. (2005) Force history dependence of receptor-ligand dissociation. Biophys. J. **88**, 1458–1466

Massin, F., Rubinstein, E., Faure, G.C., Martinet, Y., Boucheix, C. and Béné, M.C. (2004) Tetraspan and beta-1 integrins expression pattern of the epithelial lung adenocarcinoma cell line A549 and its sensitivity to divalent cations. Cytometry B Clin. Cytom. **60**, 31–36

Merilahti, P., Tauriainen, S. and Susi, P. (2016) Human parechovirus 1 infection occurs via alphaVbeta1 integrin. PLoS One, **11**, 1–17.

Meyer, C.J., Alenghat, F.J., Rim, P., Fong, J.H.-J., Fabry, B. and Ingber, D.E. (2000) Mechanical control of cyclic AMP signalling and gene transcription through integrins. Nat. Cell Biol. **2**(September), 666–668

Odorico, M., Teulon, J.-M., Bessou, T., Vidaud, C., Bellanger, L., Chen, S.W., Quéméneur, E., Parot, P. and Pellequer, J.-L. (2007) Energy landscape of chelated uranyl: Antibody interactions by dynamic force spectroscopy. Biophys. J. **93**, 645–654

Palecek, S.P., Loftus, J.C., Ginsberg, M.H., Lauffenburger, D.A. and Horwitz, A.F. (1997) Integrin-ligand binding properties govern cell migration speed through cell-substratum adhesiveness. Nature **385**, 537–540

Pincet, F. and Husson, J. (2005) The solution to the streptavidin-biotin paradox: The influence of history on the strength of single molecular bonds. Biophys. J. **89**, 4374–4381

Planus, E., Galiacy, S., Matthay, M., Laurent, V., Gavrilovic, J., Murphy, G., Clérici, C., Isabey, D., Lafuma, C. and d'Ortho, M.-P. (1999) Role of collagenase in mediating in vitro alveolar epithelial wound repair. J. Cell Sci. **112**, 243–252

Radmacher, M. (2002) Measuring the elastic properties of living cells by the atomic force microscope. Methods Cell Biol. **68**, 67–90

Rankl, C., Kienberger, F., Wildling, L., Wruss, X. Jr., Gruber, H. J., Blaas, D. and Hinterdorfer, P. (2008) Multiple receptors involved in human rhinovirus attachment to live cells. Proc. Nat. Acad. Sci. U.S.A. **105**, 17778–17783

Lo Schiavo, V., Robert, P., Limozin, L. and Bongrand, P. (2012) Quantitative modeling assesses the contribution of bond strengthening, rebinding and force sharing to the avidity of biomolecule interactions. PLoS One **7**, 1–11

Schwarz, U.S. and Gardel, M.L. (2012) United we stand - integrating the actin cytoskeleton and cell-matrix adhesions in cellular mechanotransduction. J. Cell Sci. **125**, 3051–3060

Sulchek, T.A., Friddle, R.W., Langry, K., Lau, E.Y., Albrecht, H., Ratto, T.V, DeNardo, S.J., Colvin, M.E. and Noy, A. (2005) Dynamic force spectroscopy of parallel individual Mucin1-antibody bonds. Proc. Nat. Acad. Sci. U.S.A. **102**, 16638–16643

Sun, Z., Martinez-Lemus, L.A., Trache, A., Trzeciakowski, J.P., Davis, G.E., Pohl, U. and Meininger, G.A. (2005) Mechanical properties of the interaction between fibronectin and alpha5beta1-integrin on vascular smooth muscle cells studied using atomic force microscopy. Am. J. Physiol. Heart Circ. Physiol. **289**, H2526–H2535

Tamada, M., Sheetz, M.P. and Sawada, Y. (2004) Activation of a signaling cascade by cytoskeleton stretch. Dev. Cell **7**, 709–718

Taubenberger, A., Cisneros, D.A., Friedrichs, J., Puech, P.-H., Muller, D.J. and Franz, C.M. (2007) Revealing early steps of $\alpha 2\beta 1$ integrin-mediated adhesion to collagen type I by using single-cell force spectroscopy. Mol. Biol. Cell **18**(May), 1634–1644

Teulon, J.M., Delcuze, Y., Odorico, M., Chen, S.W.W., Parot, P. and Pellequer, J.L. (2011) Single and multiple bonds in (strept)avidin-biotin interactions. J. Mol. Recogn. **24**, 490–502

Wang, N., Tytell, J.D. and Ingber, D.E. (2009) Mechanotransduction at a distance: Mechanically coupling the extracellular matrix with the nucleus. Nat. Rev. Mol. Cell Biol. **10**, 75–82

Williams, P.M. (2003) Analytical descriptions of dynamic force spectroscopy: Behaviour of multiple connections. Anal. Chim. Acta **479**, 107–115

Zamir, E. and Geiger, B. (2001) Molecular complexity and dynamics of cell-matrix adhesions. J. Cell Sci. **114**, 3583–3590

Zhang, X., Chen, A., De Leon, D., Li, H., Noiri, E., Moy, V.T. and Goligorsky, M.S. (2004) Atomic force microscopy measurement of leukocyte-endothelial interaction. Am. J. Physiol. Heart Circ. Physiol. **286**, H359–H367

Zhang, X. and Moy, V.T. (2003) Cooperative adhesion of ligand-receptor bonds. Biophys. Chem. **104**, 271–278

Received: 20 December 2016; Revised: 9 May 2017; Accepted: 11 May 2017; Accepted article online: 24 May 2017